

# Curve-Driven-Based Acoustic Inversion for Photoacoustic Tomography

Hongbo Liu, Kun Wang,\* Dong Peng, Hui Li, Yukun Zhu, Shuang Zhang, Muhan Liu, and Jie Tian\*

**Abstract**—The computation of model matrix in the iterative imaging reconstruction process is crucial for the quantitative photoacoustic tomography (PAT). However, it is challenging to establish an outstanding model matrix to improve the overall imaging quality in PAT due to the noisy signal acquisition and inevitable artifacts. In this work, we present a novel method, named as the curve-driven-based model-matrix inversion (CDMMI), to calculate the model matrix for tomographic reconstruction in photoacoustic imaging. It eliminated the use of interpolation techniques, and thus avoided all interpolation related errors. The conventional interpolated-matrix-model inversion (IMMI) method was applied to evaluate its performance in numerical simulation, tissue-mimicking phantom and in vivo small animal studies. Results demonstrated that CDMMI achieved better reconstruction accuracy until IMMI kept increasing discrete points to 10000. Furthermore, the proposed method can suppress the negative influence of noise and artifacts effectively, which benefited the overall imaging quality of photoacoustic tomography.

**Index Terms**—Photoacoustic tomography, model matrix, acoustic inversion, curve-driven, interpolated-matrix-model inversion.

## I. INTRODUCTION

**P**HOTOACOUSTIC tomography (PAT) is emerging as a fast-developing powerful noninvasive biomedical imaging

technology for the high-resolution mapping of optical absorption in scattering tissues [1-6]. In PAT, short high-power laser pulses are used to illuminate the object or region of interest, and then the pressure waves or ultrasonic waves generated from the thermal expansion are measured by ultrasound sensors that surround the imaged volume. The measured signals are used for reconstructing the distribution of the absorbed laser energy in tomographic slices.

A wide variety of algorithms have been suggested for PAT image reconstruction [7-12], which can generally be classified into three main categories: back-projection, model-based, and time-reversal methods [12]. Among them, back-projection algorithms are commonly employed due to their simplicity and ease of implementation. These algorithms are based on analytical inversion formulae and exists for several detection geometries both in time and frequency domains [13-16]. The feature of fast reconstruction speed makes them especially suitable for either 2D or 3D photoacoustic imaging requiring high temporal resolution. However, images reconstructed by back-projection algorithms usually suffer from streak-type artifacts, negative pixel intensities, as well as the loss of low-frequency information, which cause them inappropriate for imaging applications requiring accurate quantification of functional or molecular information [10], [17], [18]. Time-reversal algorithms promise more accurate reconstruction by simulating ultrasound wave propagation backward in time [19-21]. However, this process demands sophisticated numerical simulation in time domain, which may not be computationally feasible in many cases [12].

Model-based methods for PAT reconstruction model the pressure signals measured by ultrasound sensors as a linear map from the energy deposition in a grid located in the field of view (FOV) of a PAT system. Then the image reconstruction is performed by minimizing the difference between the measured signals and the signals predicted via the established photoacoustic propagation model, which is commonly depicted by a linear operator, either in time [10-12, 17, 22-26] or frequency domains [27], [28]. Different from the back-projection algorithms, there are no assumptions on the measurement geometry or the distribution of sensors in the model-based method, so they can be applied to a large variety of tomographic geometries or hardware system setups. Moreover, in such methods, the characteristics of the sensors and the variations in the speed of sound in soft tissues can be incorporated into the image reconstruction process.

In such model-based schemes of PAT reconstruction, the choice of model is crucial. If the model has too much approximations and does not preserve the inherent physical properties of the problem, the reconstructed images will not

Manuscript received April 19, 2016; revised June 18, 2016; accepted June 20, 2016. Date of publication June 23, 2016; date of current version November 29, 2016. This work is supported by the National Basic Research Program of China (973 Program) under Grant No. 2015CB755500, the National Natural Science Foundation of China under Grant No. 81227901, 61231004 and 61401462, and the Scientific Research and Equipment Development Project of Chinese Academy of Sciences under Grant No. YZ201359. The Key Research Program of the Chinese Academy of Sciences under Grant No. KGZD-EW-T03, the Chinese Academy of Sciences Fellowship for Young International Scientists under Grant No. 2013Y1GA0004 and the Project funded by China Postdoctoral Science Foundation under Grant Nos. 2014M550881, 2015T80155. Asterisk indicates corresponding author.

H. Liu, D. Peng, and M. Liu and are with the Engineering Research Center of Molecular and Neuro Imaging of the Ministry of Education and School of Life Science and Technology, Xidian University, Xi'an 710071, China and also with the Key Laboratory of Molecular Imaging, Institute of Automation, Chinese Academy of Sciences, Beijing 100190, China.

\*K. Wang is with the Key Laboratory of Molecular Imaging, Institute of Automation, Chinese Academy of Sciences; Beijing Key Laboratory of Molecular Imaging, Beijing 100190, China (e-mail: kun.wang@ia.ac.cn).

H. Li is with the College of Automation, Harbin University of Science and Technology, Harbin 150080, China.

Y. Zhu is with the School of Mechanical, Electrical and Information Engineering, Shandong University, Weihai 264209, China.

S. Zhang is with Sino-Dutch Biomedical and Information Engineering School, Northeastern University, Shenyang 110819, China.

\*J. Tian is with the Engineering Research Center of Molecular and Neuro Imaging of the Ministry of Education, School of Life Science and Technology, Xidian University, Xi'an 710071, China, and also with the Key Laboratory of Molecular Imaging, Institute of Automation, Chinese Academy of Sciences, Beijing 100190, China (e-mail: tian@ieec.org).

Color versions of one or more of the figures in this paper are available online at <http://ieeexplore.ieee.org>.

Digital Object Identifier 10.1109/TMI.2016.2584120

reflect the realistic distribution of optical absorption with sufficient accuracy. Models with high accuracy often need long inversion time and may be impractical. In A. Rosenthal *et al.*'s study [10], authors suggested a semi-analytical model-based scheme, named interpolated-matrix-model inversion (IMMI), which calculates model matrix in the time domain with a linear interpolation method and implies a piecewise planar distribution of energy deposition. After that, they modified this model to speed up the computation of the model matrix [11], [12].

However, the model matrix calculated by interpolation was not accurate enough for practical application. Thus, complicated regularization procedures had to be applied to complete the reconstruction. Therefore, in such scenarios of PAT, an accurate new model in the time domain is demanded to improve the PAT reconstruction.

In this work, we present a new approach to calculate the model matrix for accurate model-based quantitative PAT imaging, named as the curve-driven-based model-matrix inversion (CDMMI), which was inspired by the Siddon's method [29] for system matrix calculation. It has been used in the transmission or emission tomography, such as CT or PET imaging reconstructions, but to the best of our knowledge, it has not been proposed in PAT before. Our study proved that, the proposed CDMMI can calculate the model matrix of PAT with high accuracy and low time consumption. We compared our method with the accelerated version of IMMI by assessing their imaging performances with the same model matrix output in both numerical and tissue-mimicking phantom studies, as well as *in vivo* mice studies. The advantages of CDMMI were demonstrated, and its drawbacks were also discussed.

## II. THE FORWARD MODEL OF PAT

Under the condition that the duration of the employed laser pulses is shorter than the expected thermal confinement time, the heat conductance between different regions of an irradiated object can be negligible, and the acoustic sources created in the object are proportional to the absorbed optical energy. In such a scenario, neglecting acoustic losses, the acoustic pressure  $p(r, t)$  in the linear acoustic approximation and in the absence of absorption obeys [30]

$$\frac{\partial^2 p(r, t)}{\partial t^2} - c^2 \rho \nabla \cdot \left( \frac{1}{\rho} \nabla p(r, t) \right) = \Gamma \frac{\partial H(r, t)}{\partial t}, \quad (1)$$

where the sound speed  $c(r)$  and density  $\rho(r)$  vary with position  $r$ ;  $\Gamma$  is a dimensionless constant called the Grüneisen parameter, which indicates the efficiency of conversion of absorbed optical energy (heat) to pressure;  $H(r, t)$  is the heat energy per unit volume and per unit time deposited in the tissue, and in general, like the pressure  $p$ , depends on both position  $r$  and time  $t$ .

In our work, we supposed the propagation of ultrasonic waves was in an acoustically homogeneous media. Consider that the factorable  $H(r, t)$  can be expressed as the product of its spatial and temporal components, and the duration of the optical pulse was short enough to be approximated by a delta function  $\delta(t)$ , then Eq. (1) can be simplified as

$$\frac{\partial^2 p(r, t)}{\partial t^2} - c^2 \nabla^2 p(r, t) = \Gamma H(r) \frac{\partial \delta(t)}{\partial t}, \quad (2)$$

where  $H(r)$  is the spatial component of  $H(r, t)$ . After that, Equation (2) can be equivalently expressed as an initial value problem by considering the homogeneous equation [30]

$$\frac{\partial^2 p(r, t)}{\partial t^2} - c^2 \nabla^2 p(r, t) = 0, \quad (3)$$

with initial conditions

$$p(r, t)|_{t=0} = \Gamma H(r), \quad \left. \frac{\partial p(r, t)}{\partial t} \right|_{t=0} = 0. \quad (4)$$

By using the Green's function in free space [31], an analytical solution of the initial value problem in Equation (3) and (4) can be established with a Poisson-type integral [12]

$$p(r, t) = \frac{\Gamma}{4\pi c} \frac{\partial}{\partial t} \int_{S'(r, t)} \frac{H(r')}{|r - r'|} dS'(r, t), \quad (5)$$

where  $S'(r, t)$  is a time-dependent spherical surface described by  $|r - r'| = ct$ .

In a 2D geometry, for which all the sources lay in a plane, the integration was performed over a circle. Then, the surface element  $dS'(r, t)$  in Equation (5) should be replaced by the line element  $dl'$ . Suppose that the temporal profile of the pressure was in arbitrary units, then the constant term outside the derivative in Equation (5) can be neglected. Therefore, the integral in Equation (5) can be explicitly rewritten as

$$\begin{aligned} p(r, t) &= \frac{\partial}{\partial t} \int_{l'(t)} \frac{H(r')}{|r - r'|} dl'(t) \\ &= \frac{\partial}{\partial t} \int_{\theta_1(r, t)}^{\theta_2(r, t)} H(x + ct \cos \theta, y + ct \sin \theta) d\theta, \end{aligned} \quad (6)$$

where  $\theta_1(r, t)$  and  $\theta_2(r, t)$  denote angles corresponding to the two intersections between the integration curve (the circular trajectory to the ultrasound sensor with a constant distance) and the reconstructed rectangular imaging region, in which the energy deposition along each integration curve needs to be reconstructed to produce a tomographic slice.

In this work, we revealed the possibility of numerically calculating the integration in Equation (6) in 2D tomographic slices with small computational cost. Meanwhile, we proved the accuracy of the calculation depended only on the resolution of the grid, and there is not any interpolation techniques involved in the whole reconstruction process.

## III. CURVED-DRIVE-BASED MODEL MATRIX CALCULATION

In this section, the CDMMI method is described. As we mentioned previously, our descriptions are in 2D geometry, which would be suitable for tomographic slices in PAT.

### A. Model Discretization

To calculate the model matrix, which defines the mapping from the imaging object to the projections, the forward model described by Equation (6) should firstly be discretized with the

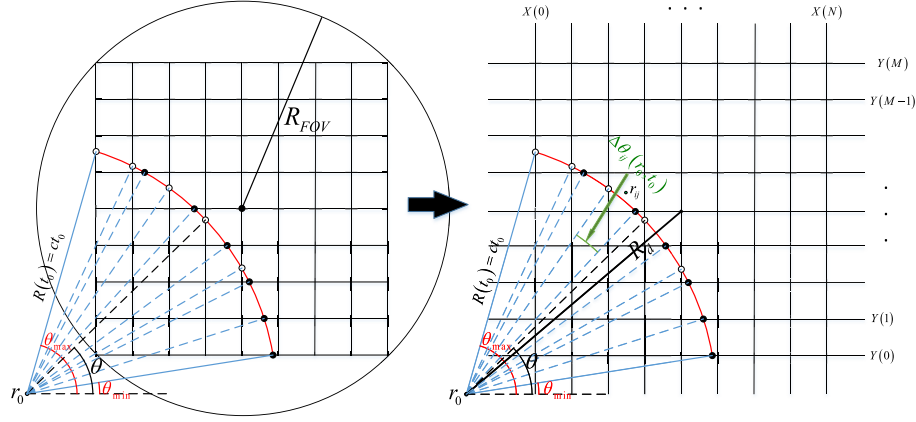


Fig. 1. Pixels of an image inside the FOV (left) can be considered as small squares in a grid formed by orthogonal straight lines crossed with a constant interval (right). Then, intersections between the integration curve and these orthogonal lines consist of two subsets: one on horizontal lines (solid circles) and the other on vertical lines (hollow circles).

finite difference method. We employed the central difference method to approximate Equation (6) as follows

$$p(r, t) \approx \frac{In(r, t + \Delta t) - In(r, t - \Delta t)}{2\Delta t} \quad (7)$$

with  $In(r, t)$  being

$$In(r, t) = \int_{\theta_1(r, t)}^{\theta_2(r, t)} H(x + ct \cos \theta, y + ct \sin \theta) d\theta. \quad (8)$$

We discretized the rectangular region containing imaging object into a grid with  $M \times N$ , so the reconstructed image also had dimensions of  $M \times N$ . We denoted the position of each pixel in the grid as  $r_{ij}$ ,  $i = 0, 1, \dots, M-1$ ;  $j = 0, 1, \dots, N-1$ , and the corresponding energy deposition was denoted as  $H(r_{ij})$ . Then Equation (8) can be discretized as

$$In(r_0, t_0) \approx \sum_{|r_{ij} - r_0| = ct_0} H(r_{ij}) \Delta\theta_{ij}(r_0, t_0). \quad (9)$$

where  $r_0$  was the position of a sensor.  $t_0$  was a time point.  $r_{ij}$  was the position of the pixel crossed by the integral curve at  $t_0$ . Therefore, the distance between the pixel  $r_{ij}$  and the sensor was  $|r_{ij} - r_0| = ct_0$ .  $\Delta\theta_{ij}(r_0, t_0)$  represented the included angle corresponding to the intersected arc inside the pixel  $r_{ij}$  (Fig. 1 green arrow), which actually was the contribution of the pixel  $r_{ij}$  to  $In(r_0, t_0)$ .

After combining Equation (7) and (9), the pressure  $p(r_k, t_l)$  measured in the location  $r_k$  at the moment  $t_l$  can be expressed as

$$p(r_k, t_l) = \sum_{i=0}^{M-1} \sum_{j=0}^{N-1} a_{ij}^{kl} H(r_{ij}), \quad (10)$$

where  $a_{ij}^{kl}$  was the entry of the model matrix.

### B. Curve-Driven Algorithm for Model Matrix Calculation

The calculation of the integration described by Equation (9) is demonstrated in this section. From now on, we simply denote  $H(r_{ij})$  as  $H_{ij}$ , the position of sensors as  $r_0 = (x_0, y_0)$  and the radius of the integration curve as  $R(t_0) = ct_0$  (Fig. 1).

Instead of being deemed as individual elements, pixels in each tomographic slice were considered as small squares in a grid formed by orthogonal straight lines crossed with a constant interval, as illustrated in Fig. 1. The integration curve intersected these lines, which resulted in two subsets of intersections, one on horizontal lines (Fig. 1, solid circles) and the other on vertical lines (Fig. 1, hollow circles). They together formed the complete intersections in this grid. Obviously, if these intersections can be traced, the entire trajectory of the integration curve can be determined. To locate them, we represented the integration curve inside a polar coordinate system as

$$\begin{cases} x(\theta) = x_0 + R(t_0) \cos(\theta) \\ y(\theta) = y_0 + R(t_0) \sin(\theta) \end{cases} \quad (11)$$

Equation (11) indicated that each intersection point between the integration curve and orthogonal lines was only related with one parameter, the angle  $\theta$ . Then,  $\Delta\theta_{ij}(r_0, t_0)$  was obtained by subtracting two sequential angles corresponding to the two adjacent intersections. After combining Equation (7), (9), and (10), the entry of the model matrix  $a_{ij}^{kl}$  can be calculated.

In the proposed CDMMI method, the model matrix was calculated in the following steps:

1) *Determine the Range of  $\theta$* : The minimal and maximal  $\theta$ , denoted as  $\theta_{\min}$  and  $\theta_{\max}$ , were calculated in the first step, which were related with the first and last intersections between the integration curve and the grid (Fig. 1). They determined the range of  $\theta$ .

2) *Calculate Angel  $\theta$* : Since all intersections can be located in the grid, their corresponding angel  $\theta$  were then calculated using Equation (11). The obtained angels should be within the range  $[\theta_{\min}, \theta_{\max}]$ .

3) *Calculate the Model Matrix*: After obtaining each  $\theta$ ,  $\Delta\theta_{ij}(r_0, t_0)$  was calculated. Then, the model matrix was solved by combining Equation (7), (9), and (10).

The detailed description of the CDMMI method is given as follows. For an image with  $M \times N$  pixels, the indices of the grid lines that may intersect with the integration curve can be

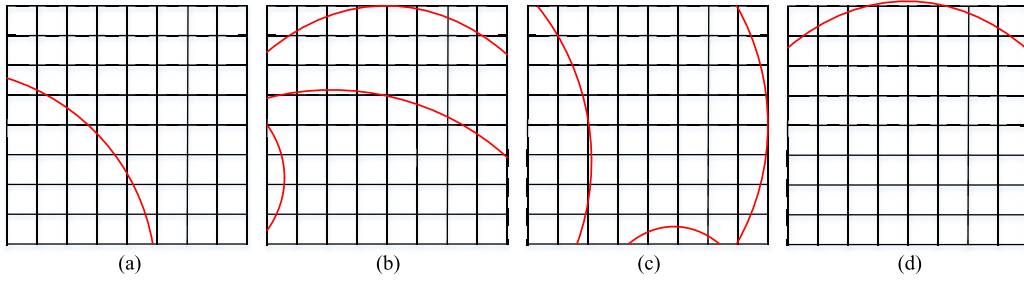


Fig. 2. Different patterns of the intersection between integration curves and the image grid. Integration curves may intersect the edges of an image two times (a, b, c), three times (b, c) or four times (d). There might be only one intersection between the integration curve and the image edge, but in this case, the intersection does not attribute itself to the measurement.

determined as follows

$$\begin{cases} |X_{line}(i) - x_0| \leq R(t_0) & (i = 0, 1, \dots, N) \\ |Y_{line}(j) - y_0| \leq R(t_0) & (j = 0, 1, \dots, M), \end{cases} \quad (12)$$

where  $X_{line}(i)$  and  $Y_{line}(j)$  were the coordinates of the orthogonal lines in  $x$ - and  $y$ -axis directions, respectively. The minimal and maximal indices in two directions were denoted as  $i_{\min}$ ,  $i_{\max}$ ,  $j_{\min}$ , and  $j_{\max}$ . Then, the  $\theta_{\min}$  and  $\theta_{\max}$  were obtained by using the following equations:

$$\begin{cases} \theta_{\min}^d = \min(2\pi, \{\theta_d^k(l) : k = 1, 2; l = i_{\min}, i_{\max}; d = x, y\}) \\ \theta_{\max}^d = \max(0, \{\theta_d^k(l) : k = 1, 2; l = i_{\min}, i_{\max}; d = x, y\}), \end{cases} \quad (13)$$

where  $\theta_d^k(l)$  were calculated as follows:

For  $x$ ,

$$\begin{cases} \theta_x^1(l) = \arccos((X_{line}(l) - x_0)/R(t_0)) \\ \theta_x^2(l) = 2\pi - \arccos((X_{line}(l) - x_0)/R(t_0)), \end{cases} l = i_{\min}, i_{\max}. \quad (14)$$

If

$$\begin{cases} R(t_0) \sin(\theta_x^k(l)) + y_0 \geq Y_{line}(M) \\ \text{or} \\ R(t_0) \sin(\theta_x^k(l)) + y_0 \leq Y_{line}(0) \end{cases}, k = 1, 2; l = i_{\min}, i_{\max}, \quad (15)$$

then  $\theta_x^k(l)$  were undefined.

For  $y$ ,

$$\begin{cases} \theta_y^1(l) = \arcsin((Y_{line}(l) - y_0)/R(t_0)) \text{ for } \theta_y^1(l) \geq 0, \\ \theta_y^1(l) = 2\pi + \theta_y^1(l) \text{ for } \theta_y^1(l) < 0, \\ \theta_y^2(l) = \pi - \arcsin((Y_{line}(l) - y_0)/R(t_0)), \end{cases} \quad (16)$$

where  $l = j_{\min}, j_{\max}$ .

If

$$\begin{cases} R(t_0) \cos(\theta_y^k(l)) + x_0 \geq X_{line}(N) \\ \text{or} \\ R(t_0) \cos(\theta_y^k(l)) + x_0 \leq X_{line}(0) \end{cases}, k = 1, 2; l = j_{\min}, j_{\max}, \quad (17)$$

then  $\theta_y^k(l)$  were undefined.

After getting  $\theta_{\min}^d$  and  $\theta_{\max}^d$ , the  $\theta_{\min}$  and  $\theta_{\max}$  were obtained with the following rules:

- 1) If an integration curve had two intersections with the image edges, which crossed a horizontal and a vertical edge, respectively (Fig. 2 a), then

$$\begin{cases} \theta_{\min} = \min(\theta_{\min}^x, \theta_{\min}^y) \\ \theta_{\max} = \max(\theta_{\max}^x, \theta_{\max}^y). \end{cases} \quad (18)$$

- 2) If an integration curve only crossed the image vertical edges (Fig. 2 b), then

$$\begin{cases} \theta_{\min} = \theta_{\min}^x \\ \theta_{\max} = \theta_{\max}^x. \end{cases} \quad (19)$$

- 3) If an integration curve only crossed the image horizontal edges (Fig. 2 c), then

$$\begin{cases} \theta_{\min} = \theta_{\min}^y \\ \theta_{\max} = \theta_{\max}^y. \end{cases} \quad (20)$$

- 4) If an integration curve crossed the image edges four times, two times with horizontal edges and two times with vertical edges (Fig. 2 d), then

$$\Delta\theta_d = \begin{cases} \theta_{\max}^d - \theta_{\min}^d & \text{for } \theta_{\max}^d - \theta_{\min}^d > \pi \\ 2\pi - \theta_{\max}^d + \theta_{\min}^d & \text{for } \theta_{\max}^d - \theta_{\min}^d \leq \pi \end{cases}, \quad d = x, y. \quad (21)$$

After combining all these cases,

$$(\theta_{\min}, \theta_{\max}) = \begin{cases} (\theta_{\min}^x, \theta_{\max}^x) & \text{if } \Delta\theta_x > \Delta\theta_y, \\ (\theta_{\min}^y, \theta_{\max}^y) & \text{else.} \end{cases} \quad (22)$$

Note that because ultrasound sensors were outside the image grid,  $\theta_{\max} - \theta_{\min} < \pi$ . Thus, if  $\theta_{\max} - \theta_{\min} \geq \pi$ , the obtained  $\theta_{\min}$  and  $\theta_{\max}$  should be adjusted, as  $\theta_{\max} = \theta_{\min}, \theta_{\min} = \theta_{\max} - 2\pi$ .

After determining the range of  $\theta$ , all  $\theta$  corresponding to the intersections between the integration curve and grid lines were calculated as follows:

$$\begin{cases} \{\theta_x\} = \{\theta_x^1(i_{\min}), \theta_x^2(i_{\min}), \dots, \theta_x^1(i_{\max}), \theta_x^2(i_{\max})\}, \\ \{\theta_y\} = \{\theta_y^1(j_{\min}), \theta_y^2(j_{\min}), \dots, \theta_y^1(j_{\max}), \theta_y^2(j_{\max})\}; \end{cases} \quad (23)$$

where

$$\begin{cases} \theta_x^1(i) = \arccos((X_{line}(i) - x_0)/R(t_0)) \\ \theta_y^1(j) = \arcsin((Y_{line}(j) - y_0)/R(t_0)). \end{cases}$$

If  $\theta_{\min} < 0$ ,

$$\begin{cases} \theta_x^2(i) = -\theta_x^1(i), \\ \theta_y^2(j) \text{ undefined}, \end{cases}$$

and

$$\begin{cases} \theta_x^1(i) \text{ undefined}, & \text{if } \theta_x^1(i) > \theta_{\max}; \\ \theta_x^2(i) \text{ undefined}, & \text{if } \theta_x^1(i) < -\theta_{\min}; \\ \theta_y^1(j) \text{ and } \theta_y^2(j) \text{ undefined}, & \text{if } \theta_y^1(j) < \theta_{\min} \text{ or } \theta_y^1(j) > \theta_{\max}; \end{cases}$$

If  $\theta_{\min} \geq 0$ ,

$$\begin{cases} \theta_x^2(i) = 2\pi - \theta_x^1(i), \\ \theta_y^2(j) = \pi - \theta_y^1(j), \\ \theta_y^1(j) = 2\pi + \theta_y^1(j), \text{ if } \theta_y^1(j) < 0, \end{cases}$$

and

$$\begin{cases} \theta_x^k(i) \text{ undefined, if } \theta_x^k(i) > \theta_{\max} \text{ or } \theta_x^k(i) < \theta_{\min}; \\ \theta_y^k(j) \text{ undefined, if } \theta_y^k(j) > \theta_{\max} \text{ or } \theta_y^k(j) < \theta_{\min}; \end{cases} \quad k = 1, 2.$$

Afterwards, the complete dataset of  $\{\theta\}$  was obtained by merging  $\{\theta_x\}$  and  $\{\theta_y\}$  together and sorting each  $\theta$  in ascending order:

$$\{\theta\} = \text{merge}\{\{\theta_x\}, \{\theta_y\}\} = \{\theta(0), \theta(1), \dots, \theta(n)\}, \quad (24)$$

which was employed to calculate all the pixels crossed by the integration curve in the next step. To achieve that, the indices of these pixels and their weights were determined as follows:

$$\begin{cases} i(m-1) = [x_0 + R(t_0) \cos(\theta_{\text{mid}}) - X_{line}(0)]/px, \\ j(m-1) = [y_0 + R(t_0) \sin(\theta_{\text{mid}}) - Y_{line}(0)]/py, \end{cases} \quad (25)$$

and

$$\Delta\theta(m-1) = \theta(m) - \theta(m-1) \quad (m = 1, 2, \dots, n), \quad (26)$$

where

$$\theta_{\text{mid}} = (\theta(m) + \theta(m-1))/2, \quad (27)$$

$px$  and  $py$  were the pixel size in  $x$  and  $y$  direction, respectively. Combining Equation (25) and (26), Equation (9) can be written as

$$\ln(r_0, t_0) = \sum_{m=1}^{n_p} H(i(m-1), j(m-1)) \Delta\theta(m-1), \quad (28)$$

where  $n_p$  was the amount of pixels crossed by the integration curve.

The procedure of solving the problem in Equation (9) is summarized in the block diagram in Fig. 3. By using this procedure to calculate  $\ln(r_0, t_0 + \Delta t)$  and  $\ln(r_0, t_0 - \Delta t)$  in terms of  $t_0 + \Delta t$  and  $t_0 - \Delta t$ , for each sensor position  $r = r_0$  and pressure measurement time point  $t = t_0$ , the non-zero entries of model matrix that correspond to pressure

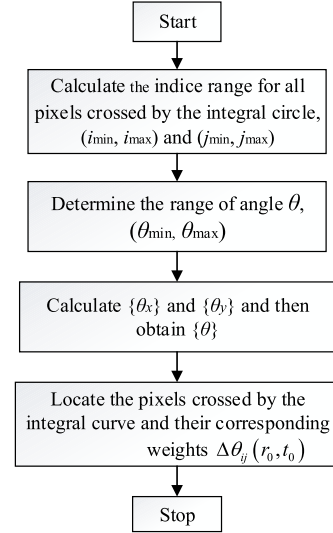


Fig. 3. Block diagram of the CDMMI method in solving Eq. (9) for PAT reconstruction.

signal  $p(r_0, t_0)$  can be finally obtained by using Eq. (7), as follows:

$$\begin{aligned} p(r_0, t_0) &= \frac{1}{2\Delta t} [\ln(r_0, t_0 + \Delta t) - \ln(r_0, t_0 - \Delta t)] \\ &= \frac{1}{2\Delta t} \left[ \sum_{m=1}^{n_1} H(i_{t_0+\Delta t}(m-1), j_{t_0+\Delta t}(m-1)) \Delta\theta_{t_0+\Delta t}(m-1) \right. \\ &\quad \left. - \sum_{l=1}^{n_2} H(i_{t_0-\Delta t}(l-1), j_{t_0-\Delta t}(l-1)) \Delta\theta_{t_0-\Delta t}(l-1) \right] \\ &= (\mathbf{M})_{r_0, t_0} \mathbf{H}, \end{aligned} \quad (29)$$

where  $(i_{t_0+\Delta t}(\cdot), j_{t_0+\Delta t}(\cdot))$  and  $(i_{t_0-\Delta t}(\cdot), j_{t_0-\Delta t}(\cdot))$  were the pixel index that crossed by the integration curve at time  $t_0 + \Delta t$  and  $t_0 - \Delta t$ , respectively, and their corresponding weights were  $\theta_{t_0+\Delta t}(\cdot)$  and  $\theta_{t_0-\Delta t}(\cdot)$ . The  $(\mathbf{M})_{r_0, t_0}$  was the row of model matrix corresponding to signal  $p(r_0, t_0)$ .

This proposed approach for calculating the model matrix in PAT reconstruction was what we called the CDMMI method. With the model matrix obtained from CDMMI, the mapping from optical absorption to measured data can be rewritten as

$$\mathbf{p} = \mathbf{M}\mathbf{H}, \quad (30)$$

where  $\mathbf{p}$ ,  $\mathbf{M}$ , and  $\mathbf{H}$  were the measured pressure data, the model matrix and the reconstructed image in a vector form, respectively. Then, the PAT reconstruction problem was equivalent to solving the following least square problem for optimization.

$$\mathbf{H}_{op} = \arg \min_{\mathbf{H}} \|\mathbf{p} - \mathbf{M}\mathbf{H}\|_2^2. \quad (31)$$

In this work, the optimization problem in Equation (31) was solved by using the LSQR algorithm [32].

#### IV. PERFORMANCE EVALUATION OF CDMMI

In this section, we demonstrate the performance of CDMMI in numerical simulations, phantom and *in vivo* studies. The CDMMI is compared with the IMMI method, which is a commonly used model-based inversion method in PAT imaging.

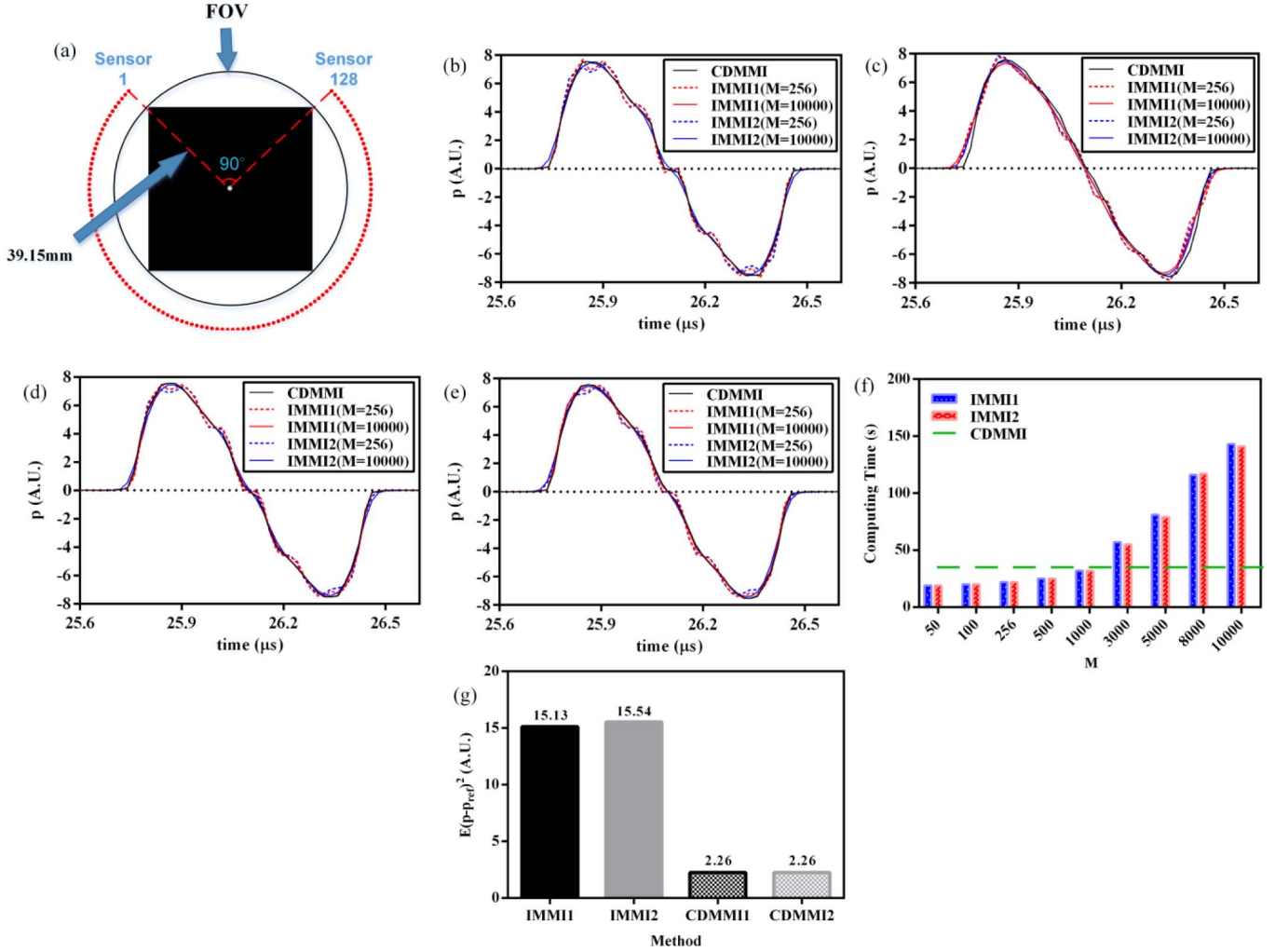


Fig. 4. The comparison of CDMMI and IMMI methods for forward numerical calculation of a point-like absorber. (a) The 128 ultrasound sensors were surrounding the absorber, which was the simulation of a commercial PAT system (iTheraMedical). (b)-(e) The calculated signals at sensor 1, 45, 87 and 122. Both linear (IMMI1) and bilinear (IMMI2) interpolations were applied in the IMMI method as references, and the discrete points were set as  $M = 256$  and  $M = 10000$ , respectively. (f) The computational time of model matrix with IMMI1 and IMMI2 are plotted in the function of discrete points. The computational time with CDMMI is marked with green dashed line. (g) The RMSE between the reference signal (IMMI with  $M = 10000$ ) and the two kinds of calculated signals (IMMI with  $M = 1000$  and CDMMI). CDMMI1 calculates RMSE between CDMMI and the reference IMMI1 with  $M = 10000$ , and CDMMI2 calculates RMSE between CDMMI and the reference IMMI2 with  $M = 10000$ .

All PAT image reconstructions were done in a laptop with four processors at 2.60 GHz and 8 GB of memory. All the algorithms were implemented by GNU c.

#### A. Simulations

To evaluate the accuracy of CDMMI for PAT imaging, two numerical phantoms were used. The first one was a point-like source. It was used to assess the forward accuracy of the model matrix obtained by CDMMI. The optical absorption distribution of the point-like source was given by

$$H(x, y) = \max \left\{ 1 - (x^2 + y^2) / 0.25, 0 \right\}, \quad (32)$$

which was discretized to a  $256 \times 256$  grid with the pixel size of  $0.1 \text{ mm} \times 0.1 \text{ mm}$ , as shown in Fig. 4 a. The pressure signal was estimated by the model matrix of 128 ultrasound sensors surrounding the center of FOV with uniform angular intervals. The radius was 39.15 mm. All these sensors covered an angle

of  $270^\circ$  round the imaging target (Fig. 4 a), which simulate the physical settings of a commercially available PAT system for small animal imaging (MOST inVision 128, iTheraMedical GmbH, Neuherberg, Germany). In this simulation, since the accuracy of IMMI highly depends on the number of discrete points, which is the density of discretization for interpolations of pixel intensity, we considered the signal estimated by IMMI with 10000 discrete points (denoted as  $M = 10000$ ) of each integration curve as the reference for comparison. Furthermore, both linear interpolation (IMMI1) and bilinear interpolation (IMMI2) were applied for the evaluation. The speed of sound was set as  $c = 1500 \text{ m/s}$ , and 1600 pressure pulses were calculated for each sensor, the sampling period was 20 ns, which corresponded to a sample frequency of 50 MHz.

The second numerical phantom mimicked a vascular structure (Fig. 5 a), which is a common application of photoacoustic imaging for *in vivo* studies. This simulation was designed to



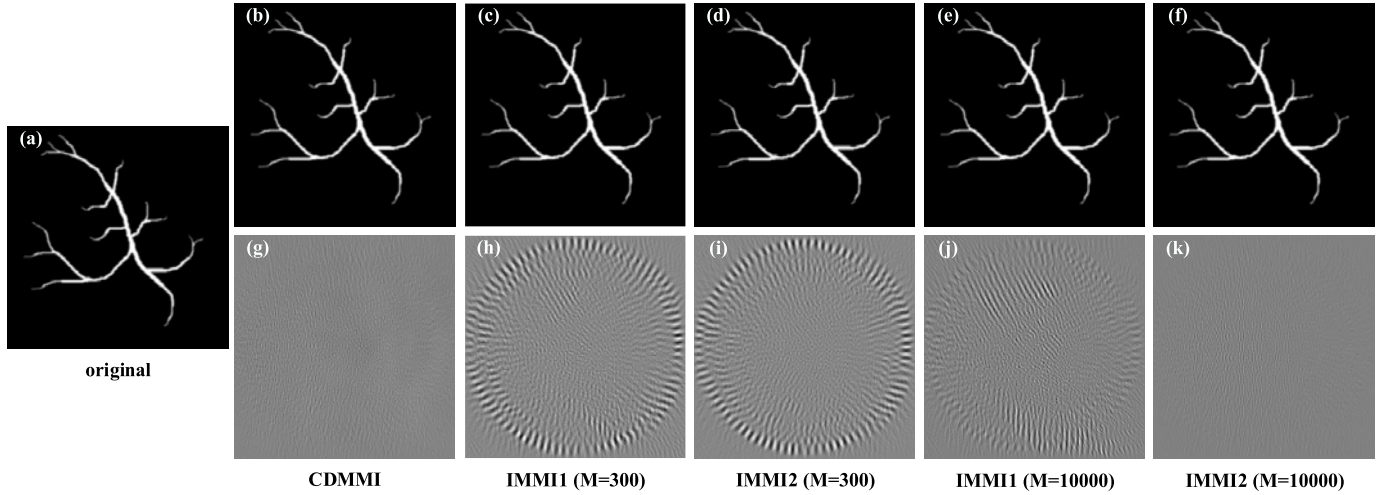


Fig. 5. Reconstruction results of blood vessels without introducing noise. (a) The original image sets up the optical absorption distribution of vessels. (b) - (f) The reconstructed images given by CDMMI, IMMI1 and IMMI2. For each IMMI method,  $M$  was set to be 300 and 10000 for reconstruction, respectively. (g) - (k) The subtraction between the original and the reconstructed images. (g) shows a similar texture as (k), but the texture of (h), (i) and (j) are distinctly different with (g) and (k).

evaluate the performance of CDMMI in both reconstruction accuracy and noise suppression. The layout of ultrasound sensors and the speed of sound were set as same as the previous simulation. To ensure the sampling frequency was high enough to avoid aliasing, the time interval between each two sampling of a sensor was set as  $\Delta t = \min(px, py)/3c$ , and thus the whole sampling time of each slice was within the range of  $[(R_d - R_{FOV})/c, (R_d + R_{FOV})/c]$ , where  $R_d$  was the distance between a sensor and the center of FOV, and in our setting it was 39.15 mm (Fig. 4 a).  $R_{FOV} = \sqrt{(M^2 py^2 + N^2 px^2)}/2$ , as shown in Fig. 1. In this case, there were  $300 \times 300$  pixels inside FOV ( $M = N = 300$ ), and the pixel size was  $0.1\text{mm} \times 0.1\text{mm}$  ( $px = py = 0.1\text{mm}$ ). So the sample frequency was 45 MHz in the time domain, and in total 1076 ultrasound pulses were detected in FOV.

### B. Phantom and in Vivo Studies

To further evaluate the performance of CDMMI, we applied it to the PAT reconstruction of a tissue-mimicking phantom and a living nude mouse. A small animal PAT system (MSOT inVision 128) was utilized to acquire the raw data, and both CDMMI and IMMI was applied to calculate modal matrices for comparisons. The MSOT inVision 128 system consisted of an optical parametric oscillator (OPO)-based laser, pumped by a Q-switched Nd:YAG laser with a pulse duration of 10 ns and repetition rate of 10 Hz. The wavelength of the laser in our experiments was set to 750 nm. The output beam was delivered by a fiber bundle divided into 10 output arms to illuminate the sample from multiple angles around the imaging plane. PA signals were acquired using a 128-element concave transducer array spanning a circle arc of  $270^\circ$ . This transducer array has a central frequency of 5 MHz and focal depth of 19 mm.

The phantom was cylindrical with a diameter of 2 cm and made of polyurethane. The shape, size and optical properties of the phantom were designed to mimic a real nude mouse (iThera Medical GmbH) [33]. Inside, there were two inner

cylindrical cavities with variations in diameter from one end to the other (Fig. 9 a). A transverse section was selected for tomographic reconstruction. In this cross-section, the diameter of one cavity was 1.5 mm, and the other was 3 mm (Fig. 9 a, reconstructed slice in red). Both cavities were filled with black india ink with the concentration by volume of 0.015%, corresponding to an optical absorption coefficient of  $1.5\text{ cm}^{-1}$ .

Six 32 days old BALB/c-type nude mice were used for *in vivo* PAT imaging in the MSOT system. All reconstructions of the targeted section were performed over a  $256 \times 256$  grid with a pixel size of  $0.1 \times 0.1\text{ mm}^2$ . In this study, to objectively comparing the anti-noise capability of different models in practical applications, the relative noise level  $\sigma_{re}$  of reconstructed images using different models were estimated with the following formula:

$$\sigma_{re} = \frac{\sigma_{im}}{\max(I)} \times 1000, \quad (33)$$

where  $\sigma_{im}$  denotes the noise level in reconstructed image  $I$ , which was estimated with the method described in [34];  $\max(I)$  was the maximal pixel value in image  $I$ .

## V. RESULTS

### A. Simulation Comparison: Forward Accuracy

The detected photoacoustic signals by four different sensors (sensor 1, 45, 87 and 122) in the point-like source simulation are shown in Fig. 4 b-e. The signal curves of CDMMI were almost overlapped with the references (IMMI1 and IMMI2,  $M = 10000$ ). However, the curve profiles of IMMI1 and IMMI2 with only 256 discrete points showed obvious deviation with the references in all four sensors. This revealed that CDMMI provided a comparable accuracy in forward calculation with the references, and it was more accurate than IMMI with  $M = 256$ . Note that based on the study of X. Luís Deán-Ben et al. [11], when the number of discrete points is equal to the size of an image, the balance

between reconstruction accuracy and computational time can be achieved using conventional model-based methods. Therefore, for IMMI, the number of discrete points was set to be the same as the image size for all comparisons. That is why we compared CDMMI and IMMI with  $M = 256$  in this case.

Inevitably, more discrete points led to more calculations for interpolation in IMMI. Fig. 4 f shows the computational time for obtaining the model matrix by each method in the function of  $M$ . Because CDMMI did not involve any interpolation process, the time consumption kept constant when image size was fixed (Fig. 4 f, green dashed line). When  $M = 1000$ , both CDMMI and IMMI consumed almost the same calculation time (IMMI1: 32, IMMI2: 32, and CDMMI: 35). But when  $M = 10000$ , the time consumption of either IMMI1 or IMMI2 was about 4 times of CDMMI (IMMI1: 143 s, IMMI2: 141 s, and CDMMI: 35 s). Fig. 4 g shows the quantitative comparison in root mean square error (RMSE) between the references (IMMI with  $M = 10000$ ) and IMMI with  $M = 1000$ , as well as between the references and CDMMI. This indicated that when both IMMI and CDMMI consumed similar time for obtaining their model matrixes, the RMSE of IMMI ( $M = 1000$ ) was more than 6-fold of the RMSE of CDMMI. CDMMI provided better forward accuracy than IMMI did while using the same computational time.

### B. Simulation Comparison: Reconstruction Accuracy

1) *Reconstruction Without Introducing Noise:* To evaluate the reconstruction accuracy of CDMMI, a simulated vascular structure without any noise was applied for the comparison (Fig. 5). After subtracting the original image and reconstructed images given by CDMMI and IMMI, the residual images of every method showed distinctly different textures (Fig. 5 g - k). It seemed that the residual images of CDMMI and IMMI2 with  $M = 10000$  had similar error textures (Fig. 5 g and k), and the rest residual images showed circular rippled textures (Fig. 5 h, i, and j), although the intensity of the rippled error texture was much lower in Fig. 5 j. It was likely that the interpolation operator in IMMI has introduced model error, thus the error in reconstructed image. These errors were  $M$  dependent. When the  $M$  increased from 300 to 10000, the errors (circular rippled textures) in the residual images faded away.

After the quantitative analysis using RMSE, as shown in Fig. 6, the CDMMI reconstruction exhibited the smallest error (the green line in Fig. 6) among all methods, which was also independent of the number of discrete points. For IMMI, by contrast, the RMSE kept decreasing with the increase of  $M$  until an optimum point. After that, increasing  $M$  did not contribute the decrease of RMSE. This phenomenon of IMMI was congruent with the findings in Ref. [11]. In this experiment, the minimal RMSE of IMMI was achieved at  $M = 3000$ . However, with  $M = 3000$ , both IMMI1 and IMMI2 showed larger errors (IMMI1: 12.81 and IMMI2: 13.05) than CDMMI did (2.75). This proved that CDMMI offered a better model matrix for more accurate PAT reconstruction.

2) *Reconstruction With Introducing Noise:* To compare the anti-noise performance between IMMI and CDMMI in PAT

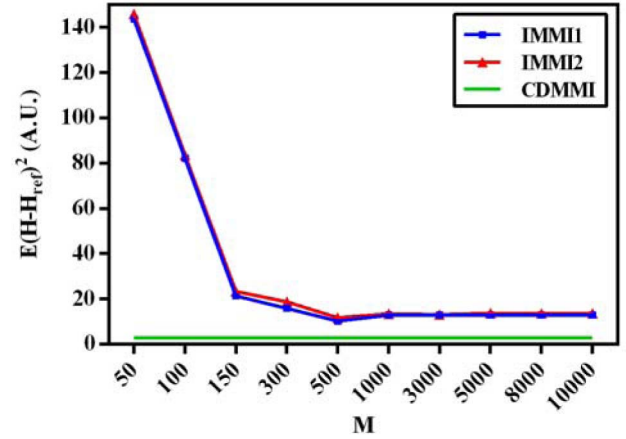


Fig. 6. Reconstruction results of the tissue-mimicking phantom in the MSOT system. (a) The schematic demonstration of the phantom. The red slice shows the location for PAT reconstruction. (b) Image reconstructed with the model matrix given by CDMMI. (c) and (d) are the reconstructed images using IMMI1 with  $M = 256$  and  $M = 10000$ , respectively. Similarly, reconstructed images using IMMI2 are shown in (e) and (f). The number of pixels was  $256 \times 256$ , which was the best setting of MSOT.

reconstruction, noise was introduced to the simulated blood vessel image with different settings of signal-to-noise ratio (SNR). Since Fig. 6 indicates that when  $M$  was greater than or equal to 300, the reconstruction accuracy of the model matrix from IMMI had very limited improvement,  $M$  was fixed to 300 for all methods in this comparison. The reconstructed images given by CDMMI, IMMI1 and IMMI2 are illustrated in Fig. 7. For the high noise and low SNR cases, such as 20% or 40% SNR, images given by CDMMI demonstrated distinctly sharper edges of the blood vessels than images reconstructed by IMMI. Furthermore, there were circular ripple artifacts appearing in the reconstructed images of IMMI1 and IMMI2, whereas images of CDMMI did not share this problem. With the increase of SNR, the differences between CDMMI and IMMI were diminishing.

The quantitative comparison of MSE also told the same story. Fig. 8 indicates that as long as the SNR was less than 50%, The RMSE given by CDMMI was only about 50-60% of that given by IMMI1 or IMMI2. For higher SNR, their accuracy tended to be similar. These measurements revealed that CDMMI was better in noise-suppression.

### C. Simulation Comparison: Time Consumption

In this study, we employed a rectangle reconstructed region of  $n \times n$  pixels, and fixed the number of discrete points to  $M = n$ . To evaluate the time efficiency for calculating model matrix by CDMMI, we measured the computational times of the model matrix with IMMI and CDMMI as a function of  $n$ . For IMMI, we also measured its time consumption with  $M = 1000$  for the comparison with CDMMI. When  $M = n$ , the computational time of the model matrix and the imaging quality was generally considered to be at the optimal balance by using IMMI [11]. Whereas when  $M = 1000$ , the IMMI and CDMMI consumed the similar amount of time for the modal matrix calculation. The results were listed in Table I.



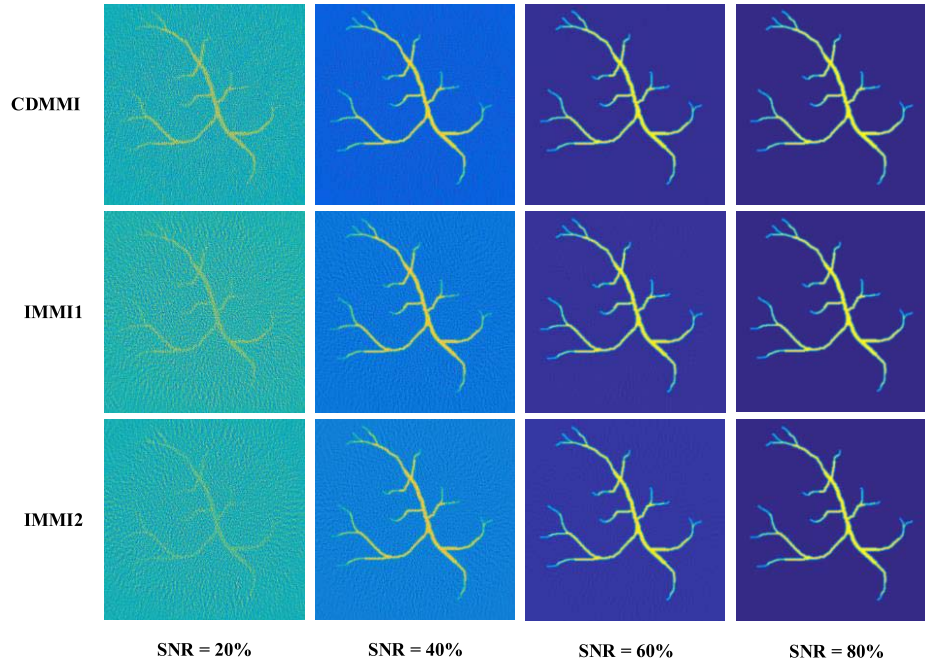


Fig. 7. The quantitative comparison between CDMMI and IMMI in reconstruction accuracy. The root mean-square-error was measured in the function of  $M$  (the number of discrete points) for IMMI1, IMMI2 and CDMMI, respectively.

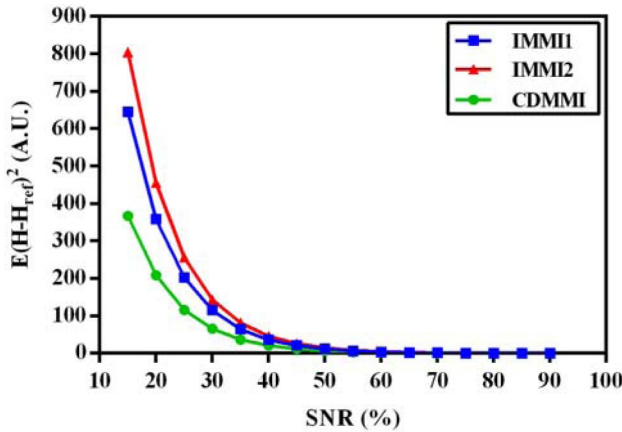


Fig. 8. The comparison between reconstructed images with different methods and SNRs. As examples, 20%, 40%, 60% and 80% SNR were applied, respectively, in order to visualize the performance of CDMMI, IMMI1 and IMMI2 for noise suppression. The  $M$  was set to be 300 in this comparison.

The number of sensors was 128, and the sampling period was 25 ns. The speed of sound was 1500 m/s in this case.

Table I shows that the computational time of CDMMI and IMMI increased with image resolution. For a PAT image with  $300 \times 300$  pixels, which is more than the most of commercialized PAT systems, averagely CDMMI only required 20 s ( $M = n$ ) and 4 s ( $M = 1000$ ) extra computational time in the comparison with IMMI. As we have demonstrated in previous simulated comparisons, CDMMI was able to provide comparable forward accuracy as IMMI even with  $M = 10000$ , and provide better reconstruction performance and anti-noise ability, if  $M = n$ . Therefore, the extra computational time was utilized to obtain a better overall imaging quality in a PAT image with larger number of pixels.

TABLE I  
COMPARISON OF THE COMPUTATION TIMES FOR MODEL MATRIX  
BETWEEN IMMI1, IMMI2 AND CDMMI

Image resolution ( $n \times n$ )	IMMI1		IMMI2		CDMMI
	$M = n$	$M = 1000$	$M = n$	$M = 1000$	
$100 \times 100$	5 s	19 s	4 s	19 s	7 s
$150 \times 150$	12 s	25 s	12 s	25 s	19 s
$200 \times 200$	16 s	29 s	16 s	29 s	28 s
$250 \times 250$	30 s	42 s	30 s	41 s	44 s
$300 \times 300$	36 s	52 s	36 s	50 s	56 s

#### D. Phantom and in Vivo Imaging Comparison

By using the MSOT system (ultrasound speed: 1475 m/s, and distance from sensors to the center of FOV: 39.15 mm), the PAT reconstruction results of the tissue-mimicking phantom are shown in Fig. 9, and the reconstruction results of the nude mouse are shown in Fig. 10. In the phantom comparisons, the image obtained using CDMMI showed sharp boundary definition of the phantom surface and two inner cavities, as well as smooth and uniform pixel intensity inside the phantom and inside the cavities. Most of the corrugated artifacts were located in the peripheral areas of the image and outside the phantom (Fig. 9 b). However, for images obtained using IMMI1 or IMMI2, no matter whether  $M$  was set to be 256 or 10000, the noise induced corrugated artifacts were found both outside and inside the phantom (Fig. 9 c-f), which affected the smoothness of the homogeneous portion of the phantom in visualization. This phenomenon confirmed the result in study [11]: More discrete points in IMMI does not improve the

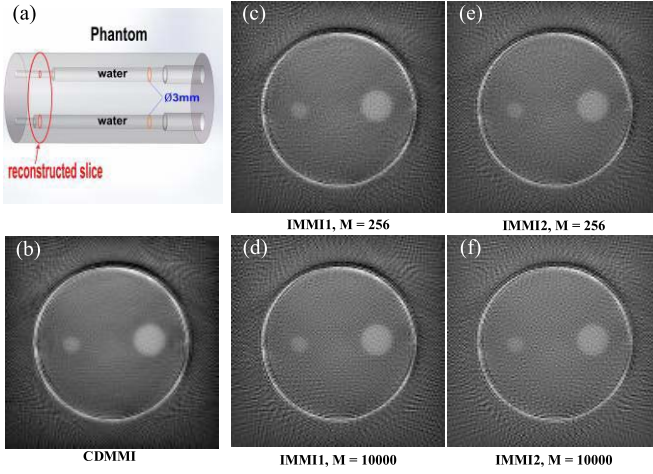


Fig. 9. The quantitative comparison between CDDMI and IMMI in anti-noise ability. RMSE was measured in the function of SNR for IMMI1, IMMI2 and CDDMI, respectively.

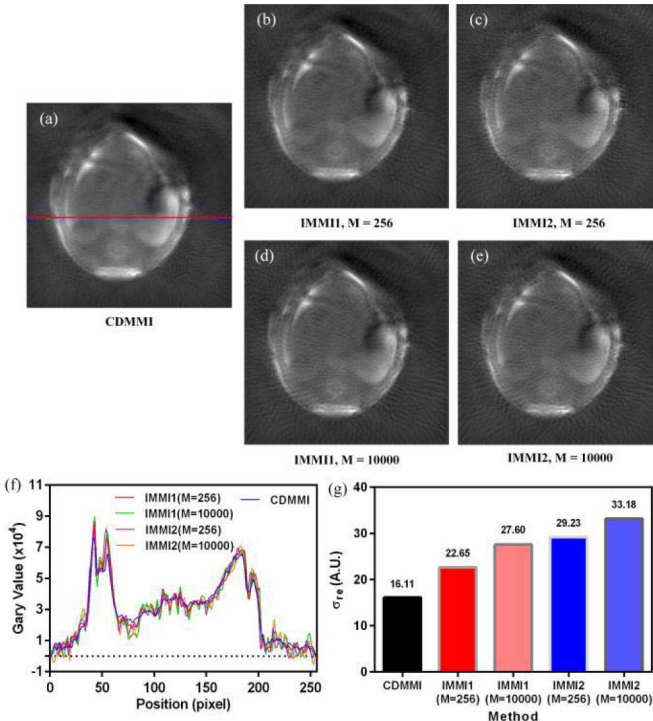


Fig. 10. Different tomographic reconstructions of a mouse in the cross-section of its kidneys. (a) Image reconstructed with the model matrix given by CDDMI. (b) - (e) are the reconstructed images using IMMI1 and IMMI2, with  $M = 256$  and  $M = 10000$ , respectively. (f) Intensity profiles extracted from the reconstructed images using different methods. The extracted position was marked by the red line in (a). The black dashed line denotes the gray value equals to 0. (g) The relative noise level of the reconstructed images using different methods. The number of pixels was  $256 \times 256$ .

smoothness in the reconstructed PAT images for homogeneous imaging objects. Fig. 9 also confirmed the results of our previous numerical simulations. Using model matrix given by CDDMI was beneficial for suppressing noise and model-error-related artifacts in PAT images.

The *in vivo* mouse imaging confirmed the same findings again (Fig. 10). As an example, the reconstructed images and

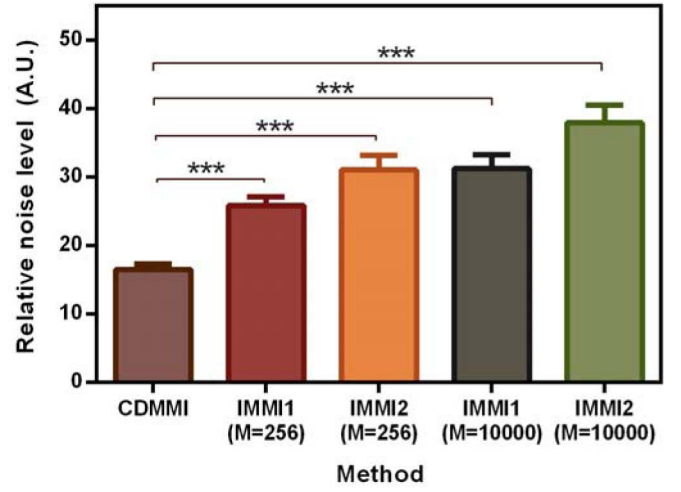


Fig. 11. Quantification of the noise level inside the reconstructed images with CDDMI and IMMI in *in vivo* experiments. Data are mean  $\pm$  s.e.m. of the relative noise level calculated from six mice reconstructed images. \*\*\*  $P < 0.001$  by Student's *t*-test.

noise analysis results of a mouse study were shown in Fig. 10. The tomographic slice obtained by CDDMI showed well defined contour of kidneys (including renal cortex and pelvis areas), spinal cord and mouse body (Fig. 10 a). The image was smooth without losing the detailed information, and also it was hardly to notice the corrugated artifacts induced by noise. However, the slices obtained by IMMI (Fig. 10 b-e) showed obvious corrugated artifacts in radial directions cross the mouse body, which blurred the details of each image. Fig. 10 f shown the intensity profiles through the kidney area in the reconstructed image given by different methods. The extracted location of the profile was marked by a red line in Fig. 10 a. The quantitative analysis of the relative noise level inside reconstructed images was shown in Fig. 10 g and Fig. 11. This verified again that CDDMI provided accurate boundary information without introducing too much noise, but the high frequency noise was not suppressed in the images reconstructed by IMMI. Interestingly, both Fig. 9 and 10 suggested that the corrugated artifacts were even enhanced in IMMI, if more discrete points were applied. We inferred that this was because of the inherent characteristics of IMMI method, which increasing  $M$  until exceeding certain threshold might not necessarily improve the overall reconstruction quality using IMMI.

## VI. DISCUSSION AND CONCLUSION

In this work, we presented a novel model-matrix calculation scheme, the CDDMI method, for model-based reconstruction in photoacoustic tomography. It was based on a convenient discretization of Poisson-type integral, which described the theoretical pressure variations due to the excitation of acoustic waves with impulse-type optical illumination. Herein, the Poisson-type integral was discretized into a weighted sum of the image pixel values which crossed by the integration curve. The weight was calculated as the included angle corresponding to the intersected arc inside the pixel crossed by the integration curve.

We conducted a series comparison between CDMMI and IMMI, which was also a model-based reconstruction method and frequently used in PAT reconstructions, through numerical simulations, tissue-mimicking phantom imaging and *in vivo* nude mouse imaging. The results proved that CDMMI can provide the same level of accuracy with IMMI in both forward and inverse calculations, if the discrete points  $M$  reached 10000. However, in this case, the computational time of IMMI was several times more than that of CDMMI. Furthermore, even with  $M = 10000$ , CDMMI showed much better ability in suppressing the noise and artifacts than IMMI did in all comparison studies. This suggests that CDMMI is more suitable for the applications in high noise and low SNR situations, which is exactly the normal imaging condition of *in vivo* PAT.

The major reason of these advantages in using CDMMI over IMMI is that it calculates the model matrix based on the direct discretization of Poisson-type integral, rather than involving interpolations. This leads to the unique ability of CDMMI in the more direct and accurate description of the relationship between the measured acoustic signals and the absorbed energy density in the tissues. Different from that, IMMI has to adopt various interpolation methods, such as linear or bilinear interpolations, to calculate the model matrix. Therefore, its reconstruction accuracy, computational time and imaging artifacts highly depends on the number of discrete points applied for interpolation, and what kind of interpolation algorithm was employed. Generally speaking, the use of interpolation in the model matrix calculation inevitably leads to worse model errors (compare with CDMMI) and instability in inverse reconstructions. Thus, in the practical image reconstructions, regularization have to be used with IMMI to suppress the model-error-related artifacts and improve the smoothness of reconstructed images. In our comparison studies, these drawbacks of IMMI were demonstrated in the manner of differentiated performance in accuracy, computational time and noise induced artifacts due to the selection of the number of discrete points and interpolation method.

It is important to calculate the model matrix with an accuracy as high as possible in a reasonable time consumption. For using about 1000 discrete points, CDMMI consumed as much computational time as IMMI did to generate the model time. This time consumption is more than that with IMMI when  $M = n$ . However, considering that CDMMI has improved the overall reconstruction performance of the model matrix distinctly, we think the payment of limited extra time is acceptable.

The disadvantage of CDMMI, as the same as IMMI, is that it is still highly image resolution dependent. For a tomographic slice consisting of more pixels, it has to consume more computational time to calculate the model matrix. However, the model matrix of CDMMI is determined only by the experimental setup, e.g., sensors' position with respect to the center of FOV, sampling frequency, etc., but not by the measured data. Thus, the model matrix only needs to be calculated once for every measurement configuration, which is particularly practical for multi-slice tomographic imaging reconstructions. Another disadvantage of the CDMMI is that

it cannot be generalized to three-dimension PAT imaging directly, which actually is our future work.

In conclusion, comparing with the conventional model-based IMMI method, the proposed CDMMI approach can improve the reconstruction accuracy, as well as reducing the influence of the noise and artifacts in photoacoustic tomography, with relatively higher calculation efficiency. This enabled CDMMI more suitable in quantitative applications of PAT requiring high accuracy.

## REFERENCES

- [1] L. V. Wang, "Multiscale photoacoustic microscopy and computed tomography," *Nature Photon.*, vol. 3, no. 9, pp. 503–509, Sep. 2009.
- [2] M. Xu and L. V. Wang, "Photoacoustic imaging in biomedicine," *Rev. Sci. Instrum.*, vol. 77, no. 4, p. 041101, Apr. 2006.
- [3] R. A. Kruger, P. Liu, Y. R. Fang, and C. R. Appledorn, "Photoacoustic ultrasound (PAUS)—Reconstruction tomography," *Med. Phys.*, vol. 22, no. 10, pp. 1605–1609, Oct. 1995.
- [4] A. Karabutov, N. B. Podymova, and V. S. Letokhov, "Time-resolved laser optoacoustic tomography of inhomogeneous media," *Appl. Phys. B, Lasers Opt.*, vol. 63, no. 6, pp. 545–563, Dec. 1996.
- [5] V. Ntziachristos and D. Razansky, "Molecular imaging by means of multispectral optoacoustic tomography (MSOT)," *Chem. Rev.*, vol. 110, no. 5, pp. 2783–2794, May 2010.
- [6] K. Wang *et al.*, "Optical molecular imaging frontiers in oncology: The pursuit of accuracy and sensitivity," *Engineering*, vol. 1, no. 3, pp. 309–323, Sep. 2015.
- [7] K. P. Kostli *et al.*, "Optoacoustic imaging using a three-dimensional reconstruction algorithm," *IEEE J. Sel. Topics Quant. Electron.*, vol. 7, no. 6, pp. 918–923, Nov./Dec. 2001.
- [8] S. J. Norton and T. Vo-Dinh, "Optoacoustic diffraction tomography: Analysis of algorithms," *J. Opt. Soc. Am. A, Opt. Image Sci. Vis.*, vol. 20, no. 10, pp. 1859–1866, Oct. 2003.
- [9] P. Burgholzer, G. J. Matt, M. Haltmeier, and G. Paltauf, "Exact and approximative imaging methods for photoacoustic tomography using an arbitrary detection surface," *Phys. Rev. E*, vol. 75, no. 4, p. 046706, Apr. 2007.
- [10] A. Rosenthal, D. Razansky, and V. Ntziachristos, "Fast semi-analytical model-based acoustic inversion for quantitative optoacoustic tomography," *IEEE Trans. Med. Imag.*, vol. 29, no. 6, pp. 1275–1285, Jun. 2010.
- [11] X. L. Dean-Ben, V. Ntziachristos, and D. Razansky, "Acceleration of optoacoustic model-based reconstruction using angular image discretization," *IEEE Trans. Med. Imag.*, vol. 31, no. 5, pp. 1154–1162, May 2012.
- [12] X. L. Dean-Ben, A. Buehler, V. Ntziachristos, and D. Razansky, "Accurate model-based reconstruction algorithm for three-dimensional optoacoustic tomography," *IEEE Trans. Med. Imag.*, vol. 31, no. 10, pp. 1922–1928, Oct. 2012.
- [13] M. Xu and L. V. Wang, "Universal back-projection algorithm for photoacoustic computed tomography," *Phys. Rev. E*, vol. 71, no. 1, p. 016706, Jan. 2005.
- [14] P. Burgholzer, J. Bauer-Marschallinger, H. Grün, M. Haltmeier, and G. Paltauf, "Temporal back-projection algorithms for photoacoustic tomography with integrating line detectors," *Inverse Problems*, vol. 23, no. 6, pp. S65–S80, Dec. 2007.
- [15] L. Zeng *et al.*, "High antinoise photoacoustic tomography based on a modified filtered backprojection algorithm with combination wavelet," *Med. Phys.*, vol. 34, no. 2, pp. 556–563, Feb. 2007.
- [16] C. G. A. Hoelen and F. F. M. de Mul, "Image reconstruction for photoacoustic scanning of tissue structures," *Appl. Opt.*, vol. 39, no. 31, pp. 5872–5883, Nov. 2000.
- [17] G. Paltauf, J. A. Viator, S. A. Prahl, and S. L. Jacques, "Iterative reconstruction algorithm for optoacoustic imaging," *J. Acoust. Soc. Am.*, vol. 112, no. 4, pp. 1536–1544, Oct. 2002.
- [18] T. Jetzfellner *et al.*, "Interpolated model-matrix optoacoustic tomography of the mouse brain," *Appl. Phys. Lett.*, vol. 98, no. 16, p. 163701, Apr. 2011.
- [19] B. E. Treeby and B. T. Cox, "k-Wave: MATLAB toolbox for the simulation and reconstruction of photoacoustic wave fields," *J. Biomed. Opt.*, vol. 15, no. 2, p. 021314, Mar./Apr. 2010.

- [20] Y. Xu and L. H. V. Wang, "Time reversal and its application to tomography with diffracting sources," *Phys. Rev. Lett.*, vol. 92, no. 3, p. 033902, Jan. 2004.
- [21] Y. Hristova, P. Kuchment, and L. Nguyen, "Reconstruction and time reversal in thermoacoustic tomography in acoustically homogeneous and inhomogeneous media," *Inverse Problems*, vol. 24, no. 5, p. 055006, Oct. 2008.
- [22] K. Wang *et al.*, "An imaging model incorporating ultrasonic transducer properties for three-dimensional optoacoustic tomography," *IEEE Trans. Med. Imag.*, vol. 30, no. 2, pp. 203–214, Feb. 2011.
- [23] K. Wang, R. Su, A. A. Oraevsky, and M. A. Anastasio, "Investigation of iterative image reconstruction in three-dimensional optoacoustic tomography," *Phys. Med. Biol.*, vol. 57, no. 17, pp. 5399–5423, Sep. 2012.
- [24] A. Buehler *et al.*, "Model-based optoacoustic inversions with incomplete projection data," *Med. Phys.*, vol. 38, no. 3, pp. 1694–1704, Mar. 2011.
- [25] L. Yao and H. Jiang, "Finite-element-based photoacoustic tomography in time domain," *J. Opt. A, Pure Appl. Opt.*, vol. 11, no. 8, p. 085301, Aug. 2009.
- [26] D. Queirós *et al.*, "Modeling the shape of cylindrically focused transducers in three-dimensional optoacoustic tomography," *J. Biomed. Opt.*, vol. 18, no. 7, p. 076014, Jul. 2013.
- [27] H. Jiang, Z. Yuan, and X. Gu, "Spatially varying optical and acoustic property reconstruction using finite-element-based photoacoustic tomography," *J. Opt. Soc. Am. A, Opt. Image Sci. Vis.*, vol. 23, no. 4, pp. 878–888, Apr. 2006.
- [28] J. Provost and F. Lesage, "The application of compressed sensing for photo-acoustic tomography," *IEEE Trans. Med. Imag.*, vol. 28, no. 4, pp. 585–594, Apr. 2009.
- [29] R. L. Siddon, "Fast calculation of the exact radiological path for a three-dimensional CT array," *Med. Phys.*, vol. 12, no. 2, pp. 252–255, 1985.
- [30] B. T. Cox, S. Kara, S. R. Arridge, and P. C. Beard, "k-space propagation models for acoustically heterogeneous media: Application to biomedical photoacoustics," *J. Acoust. Soc. Am.*, vol. 121, no. 6, pp. 3453–3464, Jun. 2007.
- [31] P. M. Morse and H. Feshbach, *Methods of Theoretical Physics*. New York, NY, USA: McGraw-Hill, 1953.
- [32] M. R. Hestenes and E. Stiefel, "Methods of conjugate gradients for solving linear systems," *J. Res. Nat. Bureau Standards*, vol. 49, no. 6, pp. 409–436, Dec. 1952.
- [33] C. J. H. Ho *et al.*, "Multifunctional photosensitizer-based contrast agents for photoacoustic imaging," *Sci. Rep.*, vol. 4, Jun. 2014, Art. no. 5342.
- [34] D. L. Donoho and J. M. Johnstone, "Ideal spatial adaptation by wavelet shrinkage," *Biometrika*, vol. 81, no. 3, pp. 425–455, 1994.